



Geophysical Research Letters

RESEARCH LETTER

10.1002/2014GL061665

Key Points:

- Complex surface mechanisms govern hydrate formation and dissociation on bubbles
- Surface hydrate morphology and coverage characteristics linked to hydrodynamics
- New mechanistic insights may have important implications for bubble plume models

Supporting Information:

- · Readme
- Text01
- Video SI-V1
- Video Animation SI-V2
- Text and Figure file SIF1toSIF23

Correspondence to:

R. P. Warzinski, robert.warzinski@netl.doe.gov

Citation:

Warzinski, R. P., R. Lynn, I. Haljasmaa, I. Leifer, F. Shaffer, B. J. Anderson, and J. S. Levine (2014), Dynamic morphology of gas hydrate on a methane bubble in water: Observations and new insights for hydrate film models, *Geophys. Res. Lett.*, 41, 6841–6847, doi:10.1002/2014GL061665.

Received 26 AUG 2014 Accepted 18 SEP 2014 Accepted article online 20 SEP 2014 Published online 13 OCT 2014

Dynamic morphology of gas hydrate on a methane bubble in water: Observations and new insights for hydrate film models

Robert P. Warzinski¹, Ronald Lynn², Igor Haljasmaa², Ira Leifer^{3,4}, Frank Shaffer¹, Brian J. Anderson⁵, and Jonathan S. Levine¹

¹National Energy Technology Laboratory, U.S. Department of Energy, Pittsburgh, Pennsylvania, USA, ²URS, South Park, Pennsylvania, USA, ³Bubbleology Research International, Solvang, California, USA, ⁴Marine Sciences Institute, University of California, Santa Barbara, California, USA, ⁵Department of Chemical Engineering, West Virginia University, Morgantown, West Virginia, USA

Abstract Predicting the fate of subsea hydrocarbon gases escaping into seawater is complicated by potential formation of hydrate on rising bubbles that can enhance their survival in the water column, allowing gas to reach shallower depths and the atmosphere. The precise nature and influence of hydrate coatings on bubble hydrodynamics and dissolution is largely unknown. Here we present high-definition, experimental observations of complex surficial mechanisms governing methane bubble hydrate formation and dissociation during transit of a simulated oceanic water column that reveal a temporal progression of deep-sea controlling mechanisms. Synergistic feedbacks between bubble hydrodynamics, hydrate morphology, and coverage characteristics were discovered. Morphological changes on the bubble surface appear analogous to macroscale, sea ice processes, presenting new mechanistic insights. An inverse linear relationship between hydrate coverage and bubble dissolution rate is indicated. Understanding and incorporating these phenomena into bubble and bubble plume models will be necessary to accurately predict global greenhouse gas budgets for warming ocean scenarios and hydrocarbon transport from anthropogenic or natural deep-sea eruptions.

1. Introduction

Vast quantities of methane and other hydrocarbon gases exist in seabed sediments on continental margins and in deep, subsea hydrocarbon reservoirs that, if released, could significantly increase global atmospheric greenhouse gas budgets [Hunter et al., 2013; Zhang et al., 2011]. Released rapidly with oil, they impact deep-sea hydrocarbon transport into multiple ecosystems [Fischer et al., 2013; Jernelöv, 2010; Thibodeaux et al., 2011].

Predicting global and regional impacts of methane and other natural gas components escaping from the seabed into deep-sea environments by natural or anthropogenic means currently is constrained by uncertainties in deep-sea bubble processes [Solomon et al., 2009]. For example, a field experiment demonstrated that deep-sea methane bubbles can become gas hydrate coated, dramatically enhancing survival, potentially allowing methane to reach surface waters and the atmosphere [Rehder et al., 2009]. That study only could posit a simplistic and seemingly nonphysical mechanism to explain the observed bubble rise velocities and decreased dissolution rates within the hydrate stability field (HSF). Details of underlying mechanisms associated with hydrate formation and stability on freely rising bubbles were unknown, preventing derivation and validation of the gas dissolution kinetics that govern bubble mass loss and transport.

Bubble dissolution kinetics are impacted by surface and trajectory oscillations and the flow field of the bubble [Clift et al., 1978]. However, most laboratory investigations of hydrate on hydrocarbon bubbles have been limited to quiescent systems or where natural bubble motions are mechanically restricted [Gumerov and Chahine, 1998; Li et al., 2013; Sun et al., 2007]. A notable exception is the seminal work by Maini and Bishnoi [1981]—with further details in Topham [1984]—where rising methane and natural gas bubbles in the range of 0.8 to 2.7 cm diameter were stabilized by a countercurrent saltwater flow, under deep-sea conditions, in a high-pressure, vertical water tunnel. Surficial hydrate formation and hydrate particle shedding were observed. A "rather naïve theoretical model" [Topham, 1984] was proposed to obtain



order-of-magnitude parameterizations of hydrate bubble processes in the HSF. More recent work on swarms of a few, small bubbles (≤3 mm diameter) in a water tunnel has indicated that a hydrate shell can exhibit different morphological features as it forms and decomposes [Chen et al., 2013]; however, clear mechanistic details were not obtained. Only a few in situ experiments have been performed on rising hydrocarbon bubbles, from which speculative models were postulated. Details of bubble hydrate formation and decomposition mechanisms either were not obtained [Rehder et al., 2002, 2009] or were obtained only for large (~5 cm diameter) bubbles that rapidly formed and shed hydrates from their trailing edge [Topham, 1978]. Such large bubbles are not commonly formed from natural seeps [Leifer, 2010].

Herein, we present results from high-speed, high-resolution video of a single rising methane bubble under deep-sea conditions that not only capture the thermodynamic and kinetics of hydrate formation and decomposition on the rising bubble in unprecedented detail but also elucidate the relationship between bubble hydrodynamics and hydrate morphology for the first time. These results were obtained from observations of a single methane bubble, surrounded and stabilized by a vertical, countercurrent flow of water in the high-pressure water tunnel facility (HWTF) at the National Energy Technology Laboratory.

2. Methods

2.1. Bubble Observation in the HWTF

Descriptions of the HWTF and its prior use with CO₂ have been published [Haljasmaa, 2006; Warzinski et al., 2008]. It is similar in design and scale to the tunnel of Maini and Bishnoi [1981] and uses a countercurrent flow of water, divergent conical inserts, and custom flow conditioning elements to stabilize a bubble, drop, or particle away from the vessel walls and near the center of a windowed viewing section (VS). The structuring of the water flow in the VS enabled extended observation of bubble motion during hydrate formation and subsequent decomposition as pressure was decreased. Turbulence intensity in the VS of the HWTF can reach 10% at maximum pump speed (~ 37 L/min); however, Moo-Young et al. [1971], in a similar, low-pressure device, noted little effect on expected air bubble shapes and rise velocities, the latter being a sensitive indicator of bubble hydrodynamics. Likewise, the design of the flow conditioning elements in the HWTF allows a bubble, drop, or particle of up to ~20 mm diameter to have sufficient freedom to permit a measure of natural hydrodynamics, in particular, lateral path and shape oscillations.

The experiment reported here involved detailed observations of a single pure methane bubble (99.99%) in fresh water prepared by reverse osmosis. The experimental temperature was 8.8 to 8.9°C. The water in the HWTF contained dissolved methane at a concentration of 0.0021 mol fraction. Elevated dissolved gas concentrations are thermodynamically required for initial hydrate formation on a bubble surface [Anderson et al., 2012]. Thermodynamic calculations, based on experimental data by Lu et al. [2008], which recently were validated in a review by Tsimpanogiannis et al. [2014], indicate that the equilibrium methane concentration for hydrate formation at the initial conditions of our experiment (8.8°C, 6.59 MPa) was 0.0018 mol fraction, similar to a MultiFlash multiphase equilibrium calculation value of 0.0017. Therefore, the HWTF was ~20% supersaturated at the beginning of this experiment. For comparison, the methane solubility in water at 8.8°C, 101.3 kPa is 0.000036 mol fraction [Gevantman, 2012].

The experiment involved three phases (see Figure 1). During Phase 1, methane was injected at constant pressure into an inverted cup in the HWTF to form a bubble of ~1 cm diameter just within the HSF at 6.59 MPa (all experimental pressures are referenced to gauge). Phase 2 started at bubble release from the cup (236 s), which occurred while increasing pressure to 10.03 MPa to promote hydrate shell formation. During Phase 3, the pressure was reduced 0.14 MPa every 60 s, which approximates the bubble's natural rise velocity. Longer intervals between pressure reductions were used when the bubble moved out of view in the HWTF, while shorter intervals were used as pressure approached the thermodynamic vapor/liquid/ hydrate (VLH) phase equilibrium point. Water velocity in the VS was determined with a high-pressure ultrasonic flow meter (Siemens Controlotron Model 1011FTN) and verified with a calibrated custom pitot tube [Lynn et al., 2014]. The bubble rise velocity was the inverse of the countercurrent flow velocity that stabilized the bubble in the viewing window of the VS. A Vision Research Phantom v341 camera was used to record both continuous high-definition (720 × 480, 30 fps) video of the bubble and high-speed, highdefinition (2560 \times 1680 at 1000 fps) video clips.

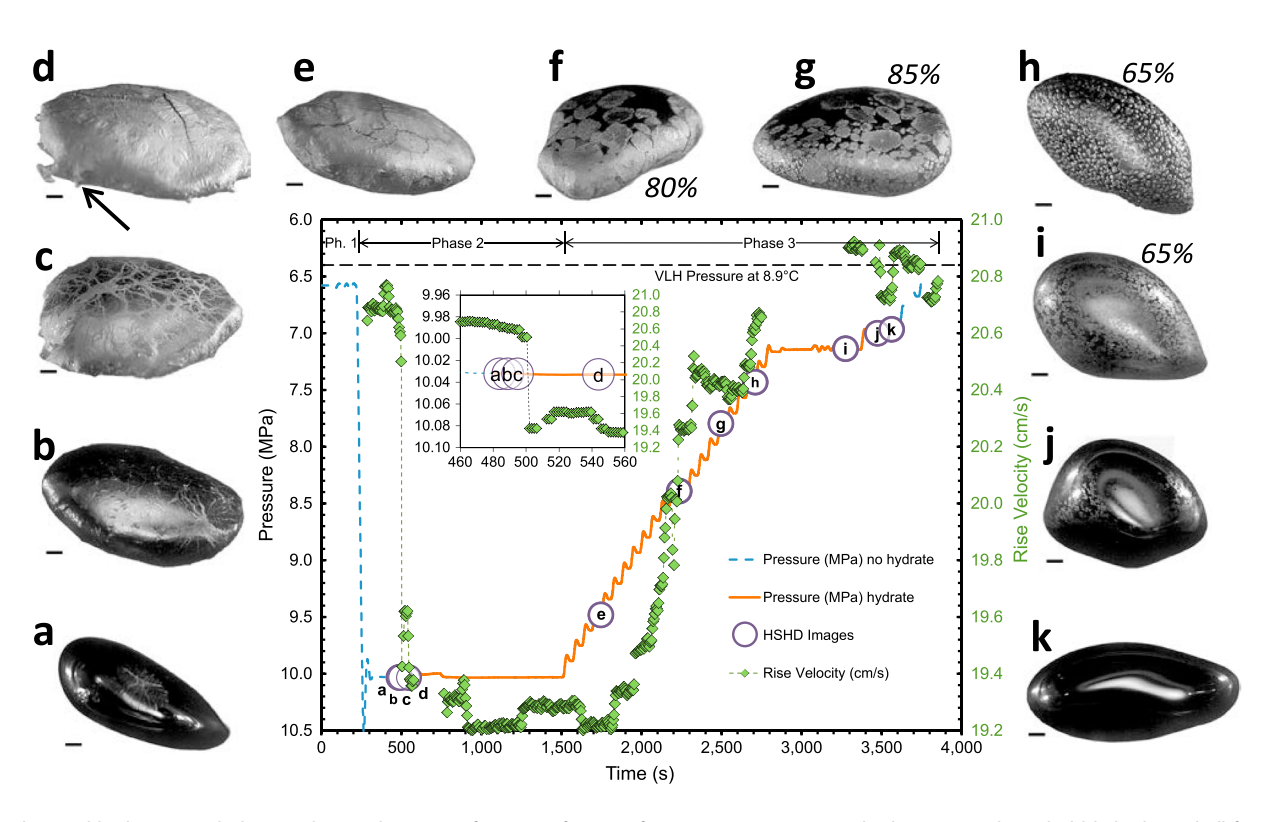


Figure 1. Observed hydrate morphology and rise velocity as a function of time, t, for a varying pressure cycle showing methane bubble hydrate shell formation and decomposition. At t = 0, the first of 68 small (~0.3 cm diameter) methane bubbles was introduced into a small inverted cup in the high-pressure water tunnel facility that rapidly coalesced to form a bubble of ~1 cm equivalent spherical diameter. The pressure scale is inverted to correspond to depth (1 MPa \approx 100 m depth). The small inset chart expands the region of initial hydrate formation. Gaps in rise velocity, i.e., no dashed line indicate intervals when the bubble moved out of view. The black horizontal dashed line indicates the thermodynamic vapor/liquid/hydrate equilibrium pressure of 6.40 MPa at 8.9°C [Sloan and Koh, 2008]. The hydrate stability field is at pressures greater than this. (a–k) Bubble images correspond to experimental times noted by lettered circles on the pressure trace. Larger, high-resolution versions of these and additional images are in the supporting information. Shown below each image are 1 mm scale bars. Arrow in Figure 1d indicates the equatorial region with thickened hydrate. Percentage of hydrate surface coverage is noted near Figures 1f, 1g, 1h, and 1i. Experimental Phases 1, 2, and 3 also are indicated; see text for details.

2.2. Hydrate Coverage

The hydrate coverage values shown in Figure 1 were obtained using a trainable segmentation technique [Arganda-Carreras et al., 2013] to recognize hydrate on the bubble interface. The hydrate-covered and hydrate-free fractions of the bubble surface then were determined with the ImageJ image processing program [Schneider et al., 2012]. Additional details and data are in the supporting information Text01 file.

2.3. Dissolution Rate

Bubble dissolution (i.e., shrinkage) rates are reported as the rate of change in equivalent spherical radius, R_e . The bubble is treated as an oblate spheroid for which $R_e = \sqrt[3]{a^2b}$, where a is the major radius and b is the minor radius, and the major radius is assumed symmetric about the minor axis. Time-averaged bubble size and shape were determined based on averaging the two-dimensional bubble edge location using 100 sequential high-definition (30 fps) video frames that fully contain the bubble. A custom National Instruments LabVIEW virtual instrument was written to automate the process.

Individual depressurization time steps in Phase 3 were too short for the determination of dissolution rate at each step; however, comparative dissolution rates were determined for several series of individual depressurization steps by applying a density correction for pressure-induced expansion of the bubble, which is reported at the average pressure and temperature for each depressurization phase. Three dissolution rates were determined during Phase 3 using this correction. The correction also was used for the two dissolution rates that were determined at constant pressure during Phase 2; however, the effect was negligible. Gas density was calculated using Multiflash (Infochem) software and the system pressure and temperature. Additional details and data are in the supporting information Text01 file.

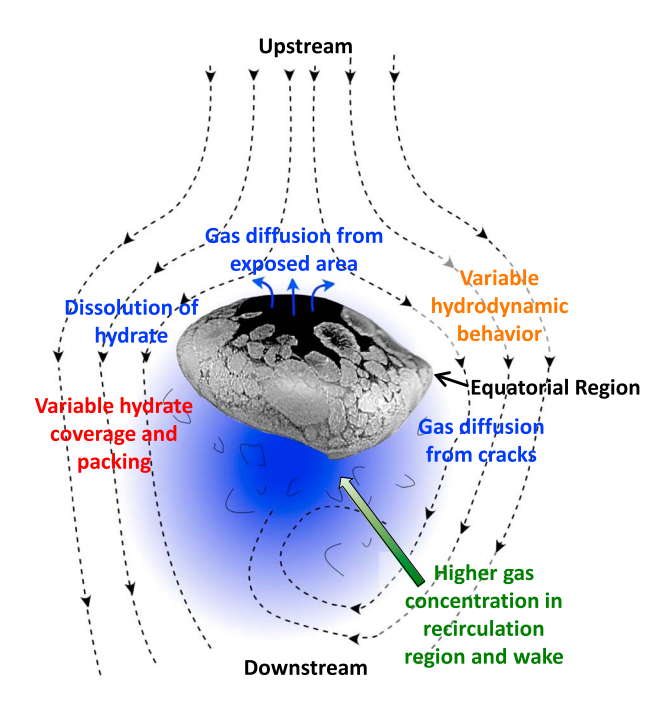


Figure 2. Schematic of bubble plume hydrodynamics and related dynamic hydrate morphology observed on a rising methane bubble. The development of new models to predict the fate of hydrate-covered bubbles in deep sea or similar environments must consider the hydrodynamic (orange text), morphological (red text), mass transfer (blue text), and thermodynamic (green text) aspects shown in this figure.

3. Experimental Observations

3.1. Hydrate Formation

Figure 1 shows an absence of hydrate during methane introduction into the bubble cup in Phase 1. After release (Phase 2), the bubble rapidly accelerated to a rise velocity of 20.7 cm/s (Figure 1). The hydrate-free bubble had a definite oscillatory motion accompanied by a surface wave that propagated around the bubble interface. Visible hydrate formation occurred after an onset time of 481 s (224 s after increase to 10.03 MPa), in agreement with onset time observations for deep-sea methane bubbles [Rehder et al., 2009]. Initial hydrate formation manifested as discrete clusters floating and growing on the bubble surface (Figure 1a and Figures SI-F1 and SI-F2 in the supporting information), which become more concentrated on and below the bubble's equatorial region. This surficial spatial distribution is consistent with the stagnant cap, bubble surfactant model where the flow constrains surficial materials to the downstream hemisphere [Johnson and Sadhal, 1985; Sadhal and Johnson, 1983]. Furthermore, hydrate formation typically

occurs at a localized, gas-saturated water interface [Sloan and Koh, 2008], which is strongest in the recirculation zone of the downstream pole area where the turbulent wake begins (Figure 2). The disconnected clusters had no obvious effect on the oscillatory motion of the bubble or the manifestation of the surface wave (Video SI-V1 and Video Animation SI-V2 at 485 s and 486 s in the supporting information).

The clusters grew for ~22 s and then fused within 2 s into a thin hydrate shell surrounding the bubble (Figures 1b and 1c and Figures SI-F3 and SI-F4, Video SI-V1 at 22 through 26 s, and Video Animation SI-V2 at 489 s and 495 s in the supporting information). The entire hydrate formation process is captured in Video SI-V1 in the supporting information. Upon shell formation, the bubble became more oblate, surface oscillations were highly dampened, and a lateral, side-to-side, rocking motion ensued. These changes resulted in an abrupt 6% decrease in rise velocity (Figure 1 inset: Point c). Similar shape and drag differences have been observed for bubbles with and without a hydrate shell, however, without mechanistic details [Sato et al., 2013].

As the shell thickened, small hydrate particles began shedding (Video Animation SI-V2 at 495 s and 510 s in the supporting information). The initial hydrate shell morphology was uneven, especially near the equator (Figures 1c and 1d and Figures SI-F4 – SI-F6 in the supporting information). However, within ~180 s, the shell became more uniform and shedding ceased (Video Animation SI-V2 at 827 s in the supporting information).

Cracks appeared in the hydrate shell within 25 s of initial hydrate formation. Correlation between surface flexing and oscillations suggests a role in hydrodynamic forcing related to these oscillations on the shell that caused cracks to open and close (Video Animation SI-V2 at 510 s and 827 s in the supporting information). These cracks are hypothesized to play a role, potentially important, in bubble gas exchange.

Dissolution rates before and after hydrate formation, expressed as the change in the equivalent spherical radius of the bubble, decreased from $0.94\pm0.05\,\mu\text{m/s}$ to $0.22\pm0.01\,\mu\text{m/s}$, in general agreement with open ocean observations [Rehder et al., 2009]. More important than the absolute values, these data and video observations demonstrate unequivocally that hydrate shell formation causes the dissolution rate decrease.



3.2. Depressurization and Hydrate Dissociation

During depressurization in Phase 3 (t > 1509 s), the hydrate is expected to dissociate as methane solubility in water in the presence of hydrate increases as the VLH equilibrium pressure is approached [Lu et al., 2008]. Decompression stresses due to gas expansion also affect the hydrate shell [Chen et al., 2013; Maini and Bishnoi, 1981], leading to increased cracking and separation of the shell into distinct, plate-like structures (Figure 1e and Figures SI-F7 and SI-F8 in the supporting information). These plates were similar in size to the fused hydrate clusters in the initial shell (Figures 1b and 1c and Figures SI-F3 and SI-F4 in the supporting information). The dissolution rate declined to $0.14 \pm 0.01 \,\mu\text{m/s}$, likely due to the lack of surface shedding.

Further depressurization was accompanied by additional morphological changes that to the best of our knowledge have not been heretofore predicted or observed. These changes in hydrate morphology were accompanied by dramatic changes in rise velocity, which, as noted, is a sensitive indicator of bubble hydrodynamics. Foremost was the separation (Figure 1f and Figure SI-F9 in the supporting information) and free movement (Video Animation SI-V2 at $t \ge 1751$ s in the supporting information) of hydrate plates, especially on the upper hemisphere, which exposed more hydrate-free bubble interface than simple cracks. Consequently, surface mobility was observed to increase in tandem with the increase in rise velocity (Figure 1). The expression of increased surface mobility also manifested in increased surface oscillations, including the surface wave previously noted. Increased surface oscillation contributed to fragmentation of the large, closely packed plates, especially in the equatorial region (Figure 1g and Figures SI-F10 – SI-F17 in the supporting information) through plate collision and abrasion, which also increased the morphological relief of the plates. Eventually, few large plates remained and the downstream hemisphere was populated mostly by smaller plates that were more loosely packed (Figure 1h and Figures SI-F18 and SI-F19 in the supporting information). At this point, rise velocity returned to values similar to those of the original, hydrate-free bubble. The average dissolution rate increased to 0.30 ± 0.01 μm/s during the depressurization steps from 2223 to 2745 s as free-gas areas were exposed on the bubble.

At 7.14 MPa, a data gap (2745-3265 s) occurred when the bubble moved out of the viewing window of the VS. Pressure was held constant during this interval. After the gap, the smaller plates in Figure 1h were visually thinner, exhibited less relief, and were more dispersed over the bubble surface (Figure 1i and Figures SI-F20 and SI-F21 in the supporting information). At this point, bubble rise velocity was similar to that of the final hydrate-free bubble (Figure 1k and Figure SI-23 in the supporting information). Hydrate coverage with partial plate coverage (Figures 1f, 1g, 1h, and 1i) was significantly less than 100% and likely dependent on both the collision/abrasion caused by the hydrodynamic motion and the thermodynamic impacts on the morphological phase rather than simply decreasing with time.

As the VLH pressure was approached, the thin plates rapidly disappeared (Figure 1j and Figure SI-F22 in the supporting information) until no visual evidence of hydrate remained (Figure 1k and Figure SI-F23 in the supporting information). The dissolution rate at this point was $0.84 \pm 0.03 \,\mu\text{m/s}$, close to the original hydratefree bubble, considering that the bubble size had changed during the course of the experiment. The experiment lasted slightly more than 1 h, comparable to the longer-lived field bubbles in Rehder et al. [2009].

4. New Insights for Bubble and Bubble Plume Modeling

The hydrate morphological changes captured in these data and their effect on bubble hydrodynamics and mass transfer build on previous lower fidelity observations. Specifically, the far higher fidelity observed here enabled more definitive elucidation of the complex controlling mechanisms than previously postulated. For example, models have been proposed to describe observations that surficial hydrate reduces, but does not halt, mass transfer through the hydrate-covering skin. Mori [1998] reviewed eight explicit models for hydrate films that he classified according to three basic assumptions causing the apparent permeability of the hydrate film: (1) the film being described as diffuse colloidal suspensions in one or more layers; (2) the film being perforated by holes, gaps, or other shapes; or (3) the film consisting of a layer of sedimented hydrate particles. Available hydrate morphology data could not validate any of these assumptions. Our direct observations of dynamic cracks in a hydrate shell (Figures 1c and 1d) confirm the second assumption. Such cracks provide a mechanism for enhancing mass exchange for hydrate-coated bubbles, even deep within the HSF, and are consistent with dynamics observed in sea ice [Smith, 2000], suggesting analogous characteristics.

More importantly, these results provide new mechanistic insights into the relationship between surficial bubble hydrate and hydrodynamics, i.e., hydrate morphological changes (continuity, thickness, flexibility, etc.) and their impact on surface tension and mobility, manifested in, among other aspects, rise velocity. Also, the role of surface oscillations on hydrate fracturing and fragmentation, especially during depressurization, is an important new insight. Again, sea ice exhibits similar morphological features [Smith, 2000] (captions of Figures SI-F6, SI-F7, SI-F9, SI-F10, and SI-F20 in the supporting information) and responds similarly to mechanical stresses of wave motion [Shen et al., 2004]. Not only do our observations validate speculative models assuming a "loose assembly" of hydrate crystals due to depressurization and hydrodynamic effects [Topham, 1984], but more importantly, they show that the hydrate surface can be far more dynamic than previously proposed.

Given the strong relationship between bubble hydrodynamics and gas exchange [Clift et al., 1978], hydrate morphology dynamics likely plays a critical role in gas exchange and dissolution rates [Rehder et al., 2009]. Thus, current models that propose a binary state of either complete or zero hydrate coverage are overly simplistic. Improved models should link gas exchange to relationships describing hydrate coverage and thickness as functions of bubble hydrodynamics and thermodynamics (Figure 2). Such models should allow not only slow hydrate dissociation with bubble rise but also free gas to escape through cracks, gaps, and larger open areas on a bubble. The limited hydrate coverage and dissolution rate data obtained from the experiment reported here indicate that an inverse linear relationship exists between hydrate coverage and dissolution rate (see Text01 in the supporting information file for more details and figures); however, this observation is preliminary pending additional experiments to study this relationship.

These different mechanisms imply distinct solubility and diffusivity dependencies. The greater surface mobility in the upper hemisphere due to a larger hydrate-free bubble surface would increase gas exchange to the bubble boundary layer (see Figure 2), which would be controlled by nonhydrate gas kinetics. Furthermore, this could decrease hydrate instability—as observed (e.g., Figure SI-F13 in the supporting information)—possibly leading to thicker hydrate plates on the bubble's downstream hemisphere.

In bubble plumes, increased bubble dissolution can decrease dissolution of trailing bubbles through enhanced plume concentrations of dissolved gas, further increasing hydrate stability on trailing bubbles, with the significance depending on bubble plume characteristics and oceanic conditions—e.g., depth and temperature [Leifer et al., 2000; Leifer, 2010]. The combined effect of thicker, more stable hydrate on the downstream side of individual bubbles and the decrease in dissolution rate of plumes is a plume synergistic feedback that enhances vertical gas transport in the ocean and couples with other plume processes, such as upwelling flow that were identified as transporting methane from the HSF to the upper ocean and even atmosphere [Solomon et al., 2009]. However, other factors, such as ambient water entrainment [Anderson et al. 2012] or detrainment of plume water by currents and other plume processes [Socolofsky and Adams, 2002], may reduce plume methane concentration. This suggests the need for modeling experiments not only to determine potential impacts but also to guide future in situ observations and larger-scale laboratory experiments.

The temporal progression of the controlling structural mechanisms documented in this study should provide a starting point for the development of new hypotheses for advancing hydrate research. These hypotheses should have testable signatures in terms of underlying controlling factors (Schmidt number dependency, solubility dependency, etc.) of bubble gas exchange and hydrodynamics. Validating and characterizing these mechanisms is key to extending the highly limited field observations globally to the world's oceans to assess the magnitude of their impact on atmospheric greenhouse gas budgets, particularly for Arctic Oceans. Furthermore, such efforts will improve predicted hydrocarbon transport from subsea blowouts and eruptions. Finally, extraterrestrial applications can be envisioned, e.g., hydrate-related phenomena on Titan and Enceladus [Prieto-Ballesteros et al., 2005; Shin et al., 2012].

Acknowledgments

We thank Michael Schellhaas and Travis Kirby for assistance in performing the experiment in the HWTF. We also thank Cantwell Carson for his help in the uncertainty and error analysis information presented here and in the supporting information and an anonymous reviewer for comments that resulted in substantial improvement in hydrate coverage and dissolution rate information in the supporting information. This work was supported by the Department of Energy Complementary Research Program under Section 999 of the Energy policy Act of 2005 and by the Department of Interior, Bureau of Safety and **Environmental Enforcement under** Interagency Agreement M11PG00053. Data used in the preparation of this work are available either from the corresponding author or J. Levine at jonathan.levine@contr.netl.doe.gov.

The Editor thanks two anonymous reviewers for their assistance in evaluating this paper.

References

Anderson, K., et al. (2012), Hydrates in the ocean beneath, around, and above production equipment, Energy Fuels, 26(7), 4167–4176,

Arganda-Carreras, I., V. Kaynig, J. Schindelin, A. Cardona, and H. S. Seung (2013), Trainable Weka Segmentation: A machine learning tool for image segmentation, Internal Rep., Dep. of Brain and Cognitive Sci., Mass. Inst. of Technol., Cambridge, Mass.

Chen, L., E. D. Sloan, C. A. Koh, and A. K. Sum (2013), Methane hydrate formation and dissociation on suspended gas bubbles in water, J. Chem. Eng. Data, 59(4), 1045-1051, doi:10.1021/je400765a.

Clift, R., J. R. Grace, and M. E. Weber (1978), Bubbles, Drops and Particles, Academic Press, New York.

- Fischer, D., J. M. Mogollon, M. Strasser, T. Pape, G. Bohrmann, N. Fekete, V. Spiess, and S. Kasten (2013), Subduction zone earthquake as potential trigger of submarine hydrocarbon seepage, Nat. Geosci., 6(8), 647–651, doi:10.1038/ngeo1886.
- Gevantman, L. H. (2012), CRC Handbook of Chemistry and Physics, 93rd ed., pp. 5-149-5-152, CRC Press, Boca Raton, Fla.
- Gumerov, N. A., and G. L. Chahine (1998), Dynamics of bubbles in conditions of gas hydrate formation, in *Proceedings of the Eighth* International Offshore and Polar Engineering Conference, edited by S. Chung et al., pp. 66-72, Montreal, Canada.
- Haljasmaa, I. V. (2006), On the drag of fluid and solid particles freely moving in a continuous medium, PhD thesis, 185 pp., Univ. of Pittsburgh, Pittsburgh, Pa.
- Hunter, S. J., D. S. Goldobin, A. M. Haywood, A. Ridgwell, and J. G. Rees (2013), Sensitivity of the global submarine hydrate inventory to scenarios of future climate change, Earth Planet. Sci. Lett., 367, 105-115, doi:10.1016/j.epsl.2013.02.017.
- Jernelöv, A. (2010), The threats from oil spills: Now, then, and in the future, AMBIO, 39(5-6), 353-366, doi:10.1007/s13280-010-0085-5.
- Johnson, R. E., and S. S. Sadhal (1985), Fluid mechanics of compound multiphase drops and bubbles, Annu. Rev. Fluid Mech., 17(1), 289-320, doi:10.1146/annurev fl 17.010185.001445
- Leifer, I. (2010), Characteristics and scaling of bubble plumes from marine hydrocarbon seepage in the Coal Oil Point seep field, J. Geophys. Res., 115, C11014, doi:10.1029/2009JC005844.
- Leifer, I., J. F. Clark, and R. F. Chen (2000), Modifications of the local environment by natural marine hydrocarbon seeps, Geophys. Res. Lett., 27(22), 3711-3714, doi:10.1029/2000GL011619.
- Li, S.-L., C.-Y. Sun, B. Liu, X.-J. Feng, F.-G. Li, L.-T. Chen, and G.-J. Chen (2013), Initial thickness measurements and insights into crystal growth of methane hydrate film, AIChE J., 59(6), 2145-2154, doi:10.1002/aic.13987.
- Lu. W., I. M. Chou, and R. C. Burruss (2008). Determination of methane concentrations in water in equilibrium with sI methane hydrate in the absence of a vapor phase by in situ Raman spectroscopy, Geochim. Cosmochim. Acta, 72(2), 412-422, doi:10.1016/j.gca.2007.11.006.
- Lynn, R. J., I. V. Haljasmaa, F. Shaffer, R. P. Warzinski, and J. S. Levine (2014), A Pitot tube system for obtaining water velocity profiles with millimeter resolution in devices with limited optical access, Flow Meas. Instrum., 40, 50–57, doi:10.1016/j.flowmeasinst.2014.08.008.
- Maini, B. M., and P. R. Bishnoi (1981), Experimental investigation of hydrate formation behaviour of a natural gas bubble in a simulated deep sea environment, Chem. Eng. Sci., 36, 183-189, doi:10.1016/0009-2509(81)80062-0.
- Moo-Young, M., G. Fulford, and I. Cheyne (1971), Bubble motion studies in a countercurrent flow apparatus, Ind. Eng. Chem. Fundam., 10(1), 157-160, doi:10.1021/i160037a027.
- Mori, Y. H. (1998), Clathrate hydrate formation at the interface between liquid CO₂ and water phases—A review of rival models characterizing "hydrate films", Energy Convers. Manage., 39(15), 1537-1557, doi:10.1016/S0196-8904(98)00029-6.
- Prieto-Ballesteros, O., J. S. Kargel, M. Fernández-Sampedro, F. Selsis, E. S. Martínez, and D. L. Hogenboom (2005), Evaluation of the possible presence of clathrate hydrates in Europa's icy shell or seafloor, Icarus, 177(2), 491-505, doi:10.1016/j.icarus.2005.02.021
- Rehder, G., P. W. Brewer, E. T. Peltzer, and G. Friederich (2002), Enhanced lifetime of methane bubble streams within the deep ocean, Geophys. Res. Lett., 29(17), 1731, doi:10.1029/2001GL013966.
- Rehder, G., I. Leifer, P. G. Brewer, G. Friederich, and E. T. Peltzer (2009), Controls on methane bubble dissolution inside and outside the hydrate stability field from open ocean field experiments and numerical modeling, Mar. Chem., 114(1-2), 19-30, doi:10.1016/i.marchem.2009.03.004.
- Sadhal, S. S., and R. E. Johnson (1983), Stokes flow past bubbles and drops partially coated with thin films. Part 1. Stagnant cap of surfactant film—Exact solution, J. Fluid Mech., 126, 237-250, doi:10.1017/S0022112083000130.
- Sato, Y., F. Kiyono, K. Ogasawara, Y. Yamaoto, T. Sato, S. Hirabayashi, and Y. Shimizu (2013), An experimental study on the dynamics of a rising methane bubble covered with hydrates, J. MMIJ, 129(4), 124-131.
- Schneider, C. A., W. S. Rasband, and K. W. Eliceiri (2012), NIH Image to ImageJ: 25 years of image analysis, Nat. Methods, 9(7), 671-675.
- Shen, H. H., S. F. Ackley, and Y. Yuan (2004), Limiting diameter of pancake ice, J. Geophys. Res., 109, C12035, doi:10.1029/2003JC002123.
- Shin, K., R. Kumar, K. A. Udachin, S. Alavi, and J. A. Ripmeester (2012), Ammonia clathrate hydrates as new solid phases for Titan, Enceladus, and other planetary systems, Proc. Natl. Acad. Sci. U.S.A., 109(37), 14,785-14,790, doi:10.1073/pnas.1205820109.
- Sloan, E. D., and C. A. Koh (2008), Clathrate Hydrates of Natural Gases, 3rd ed., 721 pp., CRC Press, Boca Raton, Fla.
- Smith, O. P. (2000), Observer's guide to sea ice, US Dept. of Commerce, National Oceanic and Atmospheric Administration, National Ocean Service, Office of Response and Restoration, National Environmental Satellite, Data, and Information Service, National Ice Center, Washington, D. C.
- Socolofsky, S. A., and E. E. Adams (2002), Multi-phase plumes in uniform and stratified crossflow, J. Hydraul. Res., 40(6), 661–672, doi:10.1080/ 00221680209499913.
- Solomon, E. A., M. Kastner, I. R. MacDonald, and I. Leifer (2009), Considerable methane fluxes to the atmosphere from hydrocarbon seeps in the Gulf of Mexico, Nat. Geosci., 2(8), 561-565, doi:10.1038/ngeo574.
- Sun, C.-Y., G.-J. Chen, C.-F. Ma, Q. Huang, H. Luo, and Q.-P. Li (2007), The growth kinetics of hydrate film on the surface of gas bubble suspended in water or aqueous surfactant solution, J. Crystal. Growth, 306(2), 491-499, doi:10.1016/j.jcrysgro.2007.05.037.
- Thibodeaux, L. J., K. T. Valsaraj, V. T. John, K. D. Papadopoulos, L. R. Pratt, and N. S. Pesika (2011), Marine oil fate: Knowledge gaps, basic research, and development needs—A perspective based on the Deepwater Horizon spill, Environ. Eng. Sci., 28(2), 87–93, doi:10.1089/
- Topham, D. R. (1978), Observations of the formation of hydrocarbon gas hydrates at depth in seawater, Catalogue No. IOS Note-4, p. 8, Institute of Ocean Sciences, Patricia Bay, Sidney, B. C., Canada.
- Topham, D. R. (1984), The formation of gas hydrates on bubbles of hydrocarbon gases rising in seawater, Chem. Eng. Sci., 39(5), 821–828, doi:10.1016/0009-2509(84)85051-4.
- Tsimpanogiannis, I. N., I. G. Economou, and A. K. Stubox (2014), Methane solubility in aqueous solutions under two-phase (H-Lw) hydrate equilibrium conditions, Fluid Phase Equilib., 371(1), 106-120, doi:10.1016/j.fluid.2014.03.012.
- Warzinski, R. P., D. E. Riestenberg, J. Gabitto, I. V. Haljasmaa, R. J. Lynn, and C. Tsouris (2008), Formation and behavior of composite CO₂ hydrate particles in a high-pressure water tunnel facility, Chem. Eng. Sci., 63(12), 3235-3248, doi:10.1016/j.ces.2008.03.005.
- Zhang, X., K. C. Hester, W. Ussler, P. M. Walz, E. T. Peltzer, and P. G. Brewer (2011), In situ Raman-based measurements of high dissolved methane concentrations in hydrate-rich ocean sediments, Geophys. Res. Lett., 38, L08605, doi:10.1029/2011GL047141.